Results in Optics 25 (2026) 101141

Contents lists available at ScienceDirect

Results in Optics

journal homepage: www.sciencedirect.com/journal/results-in-optics

Design of a non-volatile Plasmonic Memory Based on MIM waveguide and phase-change Materia for binary logic and neuromorphic integration

Melina Kehtarmanesh, Parviz Keshavarzi, Mohammad Danaie *

Faculty of Electrical and Computer Engineering, Semnan University, Semnan, Iran

A R T I C L E I N F O

Keywords:
Non-volatile memory
Plasmonic
Filter
Phase-change material
GST
Neuromorphic integration
Photonic integrated circuits

A B S T R A C T

This paper presents the design of a plasmonic memory based on Metal-Insulator-Metal (MIM) input and output waveguides and Ge2Sb2Te5 (GST) phase-change material. In this design, silver (Ag) is used as the metal, and air along with the phase-change material serve as the dielectrics. The results are reported using the Finite-Difference Time-Domain (FDTD) method. To achieve a memory structure with optimized dimensions and desired performance, a plasmonic filter has been designed. The dielectric function of the metal is characterized using the Drude theoretical model and the Johnson and Christy experimental model. The filter's transmission curve exhibits a Gaussian mode with a transmittance of 91% at the resonance wavelength of 1210 nm; the consistency between the results of the theoretical and experimental models is demonstrated in this design. Several factors were investigated and reported to assess optimal performance in the designed structure. To realize the proposed memory structure, GST material and a probe signal are utilized. This memory is programmable from above the chip and performs the reading operation of the stored state by applying a probe signal to the structure. At the resonance wavelength, this memory features a contrast of 95% and an extinction ratio of ER = 25 dB for detecting and differentiating between various states, Additionally, the Insertion Loss (IL) reading bit '1' is 0.19 dB and bit '0' is 25.2 dB, providing Footprint $= 0.095\ \mu m^2$ and 10.5 bits/μm^2 integration density. Temporal analysis of the logic state read operation is performed under excitation by a pulse with a square temporal profile distribution, and the system response is presented in terms of the normalized power $|E|^2$ as a function of time (femtoseconds). This memory cell is designed for robust binary logic operations, offering high-contrast switching for non-volatile storage in photonic integrated circuits (PICs). Furthermore, the proposed architecture serves as a foundational platform for neuromorphic integration in optical artificial neural networks (OANNs), where the multi-level crystallization potential of the phase-change material can be leveraged for future analog synaptic weight modulation.

1. Introduction

In recent years, with the accelerating growth of global data production, the demand for high-density and low-power information storage technologies has increased significantly (Wang et al., 2026). Classical electronic memory architectures, despite decades of optimization, have reached fundamental physical boundaries in scalability, speed (Jafari and Danaie, 2025b), and power density (Moon et al., 2023). These limitations highlight the necessity for novel memory technologies capable of transcending these frontiers. In this context, all-optical memories, which perform the processes of encoding, storage, and retrieval of information entirely within the optical domain, have been proposed as a promising solution (Hao et al., 2024). Photonics, utilizing light for information processing and transmission, offers high data transfer rates, low latency, and favorable energy efficiency, which has driven the demand for research into optical and photonic memory technologies (Pugachov et al., 2024). Among the established approaches, memories based on Phase-Change Materials (PCMs) have secured a unique position due to their ability for reversible transitions in crystalline structure and optical properties. Integrating these materials with plasmonic nanostructures has enabled the development of a new generation of high-speed, nanometric single-bit and multi-level optical memories (Bhatt et al., 2024).

The implementation of all-optical memories is associated with numerous challenges. Silicon-on-Insulator (SOI) platforms are CMOS-compatible but suffer from high losses and limited integration (Nikitin

* Corresponding Author.
E-mail address: danaie@semnan.ac.ir (M. Danaie).

https://doi.org/10.1016/j.rio.2026.101141
Received 3 May 2026; Received in revised form 2 August 2026; Accepted 31 August 2026
Available online 6 September 2026

et al., 2022). Localized Surface Plasmon Resonance (LSPR) concentrates the field but is limited by Ohmic losses and fabrication complexity (Haokang et al., 2025). Laser-Induced Surface Plasmon Polaritons (LASP) are high-speed but sensitive to fabrication defects and thermal management (Sun et al., 2025). Photonic crystals offer advantages through the control of light propagation and high quality factors, yet they are limited by tunability and fabrication precision (Park and H, n. d.). Kerr materials, through nonlinear effects, enable multi-level memory and reconfigurability but require high optical intensities and are sensitive to noise (Galoppo et al., 2025). In contrast, Phase-Change Materials (PCMs) enable data retention even after the light source is disconnected due to their non-volatile storage and high optical contrast, although they face challenges such as low crystallization speed and cyclic degradation (Ehrmann et al., 2022). Slow-light enhancement strengthens light-matter interaction but suffers from limited bandwidth and insertion losses (Pan et al., 2024). Finally, Semiconductor Optical Amplifiers (SOAs) provide high gain but are limited by polarization sensitivity and saturation constraints (Cui et al., 2021).

Plasmonics, due to its unique ability to confine and control electromagnetic fields at sub-wavelength scales, has become a key platform for the development of integrated optical components (Mcoyi et al., 2025). In this regard, the Metal-Insulator-Metal (MIM) waveguide structure, characterized by high confinement, precise tunability, and compatibility with photonic integrated circuits, is considered one of the prominent architectures (Zayets et al., n.d.). It is employed in the design of various components, including filters (Zegaar et al., 2022), sensors (Rahad et al., 2024), photodetectors (Oshita et al., 2023), optical switches [19], demultiplexers (Wang et al., 2023), Mach-Zehnder interferometers (Jiang et al., 2018), power amplifiers (Haffner et al., 2015), and memories [23]. Research in the field of plasmonics remains both attractive and challenging, paving the way for the advancement of nanophotonic technologies.

In recent years, plasmonic memories based on Phase-Change Materials (PCMs) have emerged as a new generation of nonlinear optical devices (Shen et al., n.d), enabling the combination of non-volatile storage functionality with a tunable optical response (Dolatabady and Granpayeh, 2015). These phase-change-based plasmonic structures, by utilizing localized surface resonances and phase-change dynamics at the nanoscale, provide a suitable platform for implementing plasmonic neuromorphic synapses (Song et al., n.d.). In such architectures, synaptic weights are tunable through optical excitation and material phase transitions, enabling adaptive learning, analog weight adjustment, and parallel data processing (He et al., 2024). This strategy represents a fundamental step toward achieving all-optical neuromorphic computing and the simultaneous integration of logic and memory into a single photonic platform (Nohoji et al., 2025a).

In recent years, significant advances in neuromorphic photonics have opened new pathways toward the realization of brain-inspired computing systems capable of overcoming the limitations of conventional von Neumann architectures (Wang et al., 2026). In these systems, optical signals are exploited to emulate the behavior of biological synapses, enabling ultra-fast, parallel, and energy-efficient information processing (Ahmadivand et al., 2017; Nohoji et al., 2026). A fundamental requirement in this field is the ability to achieve dynamic and reversible tunability of synaptic weights in the optical domain. Phase-change materials, particularly GST, have emerged as highly promising candidates due to their non-volatile and reversible transition between amorphous and crystalline states, accompanied by pronounced variations in refractive index and absorption [19]. By integrating these materials into nanoscale plasmonic structures, the light–matter interaction can be significantly enhanced, enabling precise modulation of optical transmission. This phase-dependent optical response can be directly mapped onto synaptic weight variation, thereby making plasmonic phase-change platforms strong candidates for realizing compact, scalable, and fully optical neuromorphic photonic systems (Song et al., n.d.).

Phase-change materials (PCMs) refer to a class of materials capable of reversible transitions between two structural, electronic, or optical states. These materials are classified based on the type of thermal, electronic, spin, or ionic excitation and the mechanism of their phase transition (Nohoji et al., 2025b): GST alloys (Wang et al., 2023) Materials with Metal-Insulator Transitions (MIT) (Redaelli et al., 2022) Spin-transition-based materials (Qu et al., 2017) Ion-based bistable materials (Haddad et al., 2022) Phase-change polymer compounds (Zhang et al., 2018).

Recent studies have explored various strategies to enhance PCM performance, ranging from material-level engineering—such as chemical doping—to device-level structural design. For instance, (Yao et al., 2021) demonstrated that Zn-doping in GST significantly improves thermal stability and crystallization kinetics. Building upon these material-level advancements, our work shifts the focus to device-level optimization by utilizing a dumbbell-shaped MIM plasmonic resonator to achieve extreme sub-wavelength confinement and field enhancement.

In the design of plasmonic memories, optical pulses are utilized as input signals. Each input signal possesses specific characteristics. The programming signal contains SET and RESET pulses; applying this signal to the material alters its microscopic structure, referring to the phase transition from the amorphous state to the crystalline state and vice versa (Prajapati and Kandasubramanian, 2020). When the GST material is in the amorphous state, a SET pulse characterized as a slow laser pulse with low power (amplitude) and a relatively long duration is applied. By decreasing resistance and increasing the refractive index, the material transforms into the crystalline state. In the crystalline state, a RESET pulse, a fast laser pulse with a relatively short duration and high power (amplitude) is applied to the GST material. By increasing resistance and decreasing the refractive index, the material converts back to the amorphous state (Wang et al., 2012; Sreekanth et al., 2021). In Fig. 1(a), the excitation of GST with SET and RESET optical pulses causes an atomic structure rearrangement and induces a phase transition, which creates phase-dependent modulation of the refractive index and precise variations in absorption. The spectral curves of the real refractive index (n) and the imaginary part (k) in Figs. 1 (b, c) compare the amorphous and crystalline phases. In the amorphous phase, n and k are positive and $n > k$, indicating lower absorption and a lower refractive index, while in the crystalline phase, the simultaneous increase in n and k enhances scattering and absorption, increasing the optical response of the material (Sreekanth et al., 2021).

Unlike passive materials such as silicon, the GST phase-change material is an active medium that can be utilized to implement active plasmonic devices. This material exhibits the capability for reversible refractive index transitions between the amorphous and crystalline states at telecommunication wavelengths (Ruhul Fatin et al., 2024; Butt, 2025; Pomianowski et al., 2013; Gupta et al., 2025). This phase transition leads to fundamental changes in the effective dielectric constant of the material, arising from the transformation in the band structure and the electronic density of states (Wang et al., 2019).

Table 1 lists the optical and thermal properties of the materials used in this design. The density and thermal stability of this material enable its efficient integration into photonic integrated circuits (PICs) for the development of all-optical devices with high energy efficiency (Kang et al., 2021).

The phase transition mechanism in the GST material is inherently photothermal; the switching process between the amorphous and crystalline phases depends on the temperature dynamics of the material (Zareizadeh and Nozhat, 2023). In our FDTD framework, these phase transitions are modeled by applying the corresponding complex refractive indices (n and k) for the amorphous and crystalline states. This approach is physically justified for assessing the photonic performance of the integrated circuit, as the optical response is directly determined by the material's refractive index once the stable phase is established.

The reversible phase transition of the GST layer is driven by controlled photothermal excitation. In accordance with the thermal kinetics reported in (Zareizadeh and Nozhat, 2023) and the energy

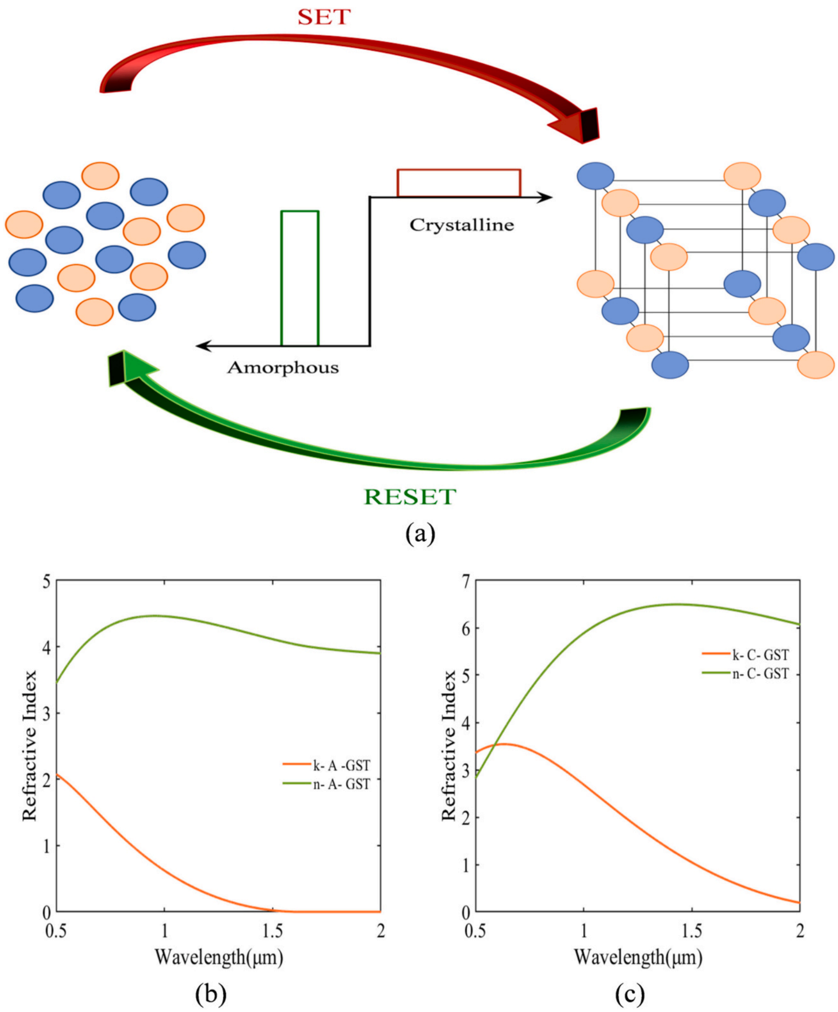

Fig. 1. (a) Atomic structure transformation under optical pulse excitation; Spectral curves of real and imaginary refractive indices for (b) Amorphous and (c) Crystalline states.

Table 1
Mechanical and Thermal Properties of Utilized Materials (Kang et al., 2021)

Material	$\tilde{n}$	$C_p \left[\frac{J}{K}\right]$	$K \left[\frac{W}{mK}\right]$	$\delta \left[\frac{Kg}{m^3}\right]$
$GST_{crystalline}$	$6.11^* + 0.83i^*$	210	0.8	6200
$GST_{amorphous}$	$3.94^* + 0.045i^*$	210	0.3	6150
Ag	$0.145 + 11.445i$	235	420	10,490
Air	$1 + 10^{-10}i$	1005	0.024	1.2

*Temperature-dependent parameters; reported values measured at room temperature.

conversion metrics defined in (Gemo et al., 2019), the GST layer must reach a crystallization temperature of $T_c \approx 450$ K for the SET process and a melting temperature of $T_m \approx 880$ K for the RESET process. Accordingly, the SET operation is triggered by an optical pulse of 50 mW for 150 ns (~7.5 nJ), allowing sufficient time for atomic rearrangement. Conversely, the RESET operation is achieved through a higher-power pulse of 110 mW for 20 ns (~2.2 nJ), facilitating rapid melting and quenching. These pulse parameters ensure precise control over the phase state, bridging our photonic simulation framework with established thermal and electrical characterization data.

Recent progress in phase-change materials has focused on both material-level engineering and device-level architectures. For instance, studies on Bi-doped Zn—Sb alloys have demonstrated that spinodal decomposition can facilitate controlled transitions through intermediate resistance states, offering a robust strategy for multi-level data storage (Chen et al., 2017). Building upon these advancements in material physics, our work focuses on the device-level optimization of photonic memories. We propose a dumbbell-shaped MIM plasmonic resonator that leverages extreme sub-wavelength field confinement to achieve high-contrast switching, providing a versatile platform that is inherently compatible with these multi-level phase-change dynamics.

In this paper, a novel all-optical plasmonic memory architecture based on phase-change materials is designed with the aim of overcoming the limitations of conventional technologies. Plasmonic memories based on GST material are categorized under Phase-change Random Access Memory (PRAM) and Non-Volatile Random Access Memory (NVRAM) (Zhang et al., 2012). The proposed structure consists of plasmonic waveguides coupled to a resonator containing phase-change material and is engineered such that the operating bandwidth, spectral response, and optical behavior of the system can be effectively controlled by tuning the coupling distance and resonator dimensions.

A comprehensive analysis of key performance parameters, including resonance wavelength, optical contrast, Extinction Ratio (ER), footprint, and storage density, has been performed using the Finite-Difference Time-Domain (FDTD) methods, demonstrating optimal results in terms of stability and optical efficiency. Simulation results indicate that the designed structure can function as a dynamically tunable plasmonic filter between band-pass and band stop states, a non-volatile single-bit plasmonic memory, and a programmable neuromorphic synapse. This multi-functional capability makes the proposed architecture a suitable candidate for integration into compact and low-power photonic chips, providing an efficient framework for realizing next-generation photonic neuromorphic computing.

The content presented in this paper is organized as follows: Section two: Design Methodology Section three: Design of the Plasmonic Filter Structure Section four: Design and Performance Analysis of the Non-Volatile Plasmonic Memory based on Phase-Change Material, Section five: Neuromorphic Photonic Performance and Time-Domain Analysis, Section six: Fabrication and Structural Integration, Conclusion of findings and elucidation of the technology's applications in neuromorphic computing.

2. Design methodology

SPPs emerge at metal-dielectric interfaces through the coupling of electromagnetic waves with a metal's free electrons. The dispersion relation for the fundamental surface plasmon TM mode can be obtained as follows (Wang et al., 2020):

$$K_{spp} = \sqrt{\frac{\varepsilon_d \varepsilon_m(\omega)}{\varepsilon_d + \varepsilon_m(\omega)}}\ \frac{\omega}{c} \tag{1}$$

In Eq. (1), k_{SPP} is the plasmonic wave vector, $\varepsilon_m(\omega)$ is the permittivity of the metal, ε_d is the permittivity of the dielectric and c is the speed of light in vacuum. The optical response of noble metals such as silver and gold in plasmonic nanostructures has been modeled using the Drude formalism Eq. (2), which describes the free-electron behavior across visible and infrared spectral regimes. $\varepsilon(\omega)$ is the complex dielectric function, ε_∞ is the high-frequency dielectric constant, ω_p is the plasma frequency, γ is the damping constant and $\omega = \frac{2\pi c}{\lambda}$ is the angular frequency of the incident light [49,50].

$$\varepsilon(\omega) = \varepsilon_\infty - \frac{\omega_p^2}{\omega^2 + i\gamma\omega} \tag{2}$$

In Eq. (2), ε_∞, representing the dielectric constant of metals at high frequencies, exhibits a value approaching unity. By incorporating intrinsic loss mechanisms, it achieves superior accuracy compared to the Drude model. The complex dielectric constant of silver is thereby determined (Maier, 2007),

$$\varepsilon(\lambda) = \varepsilon_{real}(\lambda) + i.\varepsilon_{imag}(\lambda) \tag{3}$$

with its real part $\varepsilon_{real}(\lambda) = n^2(\lambda) - k^2(\lambda)$ and imaginary part $\varepsilon_{imag}(\lambda) = 2n(\lambda)k(\lambda)$ components being precisely computed through this formulation (Blakemore, 1985).

$$2in(\omega)K(\omega)K^2(\omega) - n^2(\omega) = [n(\omega) + iK(\omega)]^2 = \varepsilon(\omega) \tag{4}$$

The optical response of the plasmonic filter at wavelength λ can be calculated by combining experimental data from Johnson and Christy with Maxwell's equations, as described by Eq. (5). E is the electric field, μ is the magnetic permeability and $\omega = \frac{2\pi c}{\lambda}$ is the angular frequency of the incident light (Johnson and Christy, 1972).

$$\nabla \times \left(\frac{1}{\mu}\nabla \times E\right) - \omega^2\varepsilon(\lambda)E = 0 \tag{5}$$

To evaluate the performance of plasmonic filters, it is essential to calculate two key parameters the FWHM and the quality factor, which are presented in Eqs. (6) and (7), respectively. λ_H is the high wavelength, λ_L is the low wavelength and λ_0 is the central resonance wavelength (West et al., 2010).

$$FWHM = \lambda_H - \lambda_L \tag{6}$$

$$Q = \frac{\lambda_0}{FWHM} \tag{7}$$

Thus far, the theoretical foundations and fundamental formulations governing the phenomenon of surface plasmons have been briefly reviewed. Additionally, the essential equations required for evaluating and validating the performance of plasmonic filters have been precisely presented. Next, the design details and specifications of an advanced single-mode plasmonic filter are examined, which leverages the unique capabilities of surface plasmons for precise light control.

3. Plasmonic filter design

In this paper, a non-volatile plasmonic memory based on Metal-Insulator-Metal (MIM) input and output waveguides and Ge2Sb2Te5 (GST) phase-change material is proposed. To achieve a structure with desired performance and optimized dimensions, a single-mode plasmonic band-pass filter has been designed, and the results are investigated and reported. In this filter design, silver (Ag) is utilized as the metal and air serves as the dielectric. The Drude model is employed to characterize the dielectric function of the metal, and the results are reported using the two-dimensional (2D) FDTD method.

In the simulation, a Gaussian pulse with the capability of exciting the Transverse Magnetic (TM) mode is used as the light source, which is applied to the structure via the input waveguide. To enhance simulation accuracy, a mesh size of 3 nm and Perfectly Matched Layer (PML) regions are utilized to model infinite space.

The topology of the single-mode plasmonic bandpass filter structure is illustrated in Fig. 2. This filter is based on MIM input and output waveguides and a rectangular resonator surrounded by two semi-disk resonators. The dimensions of the variable parameters for this design are provided in Table 2. This filter is classified as a passive plasmonic device.

The transmission curve of this filter within the 1000–1500 nm wavelength range is shown in Fig. 3. The filter exhibits a Gaussian transmission spectrum with a transmittance of 91% at the central wavelength of 1210 nm. Using eqs. (6), the Full Width at Half Maximum (FWHM) was calculated to be 56 nm, Using eqs. (7), the Quality factor (Q) was determined to be 21, respectively.

Optimizing the geometric dimensions of the variable parameters plays a critical role in achieving these enhanced performance metrics. In this study, a Parametric Sweep Simulation (PSS) approach was implemented to identify the ideal structural dimensions. During this procedure, the dimension of a single target parameter is swept across a specified range using designated step sizes, while all other structural parameters remain fixed. Crucially, to ensure that geometric variations are accurately reflected in the output response, the incremental step size of the swept parameter must be an integer multiple of the predefined mesh grid size (Δx) within the simulation domain, and must never fall below this spatial resolution limit (Palik, 1998).

Fig. 4 illustrates the transmission curves as a function of variations in three parameters: R, D, and L, within the wavelength range of 1000–2500 nm. In Fig. 4(a), the 3D transmission curve is shown as the radius of the semi-disk resonator (R) increases from 240 to 360 nm with a step size of 6 nm. It is observed that increasing the radius results in a

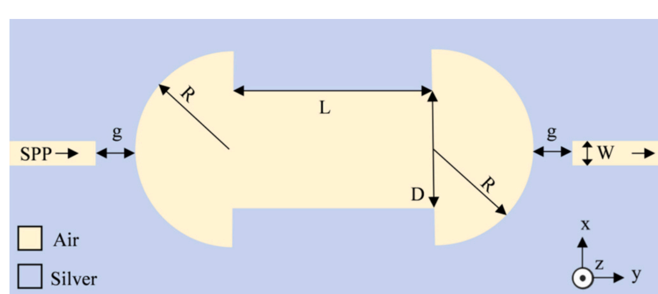

Fig. 2. Schematic of the proposed single-mode plasmonic band-pass filter structure.

Table 2
Dimensions of Variable Parameters for the Plasmonic Filter.

Parameter	R	D	L	g	w
Dimensions (nm)	300	270	500	0	50

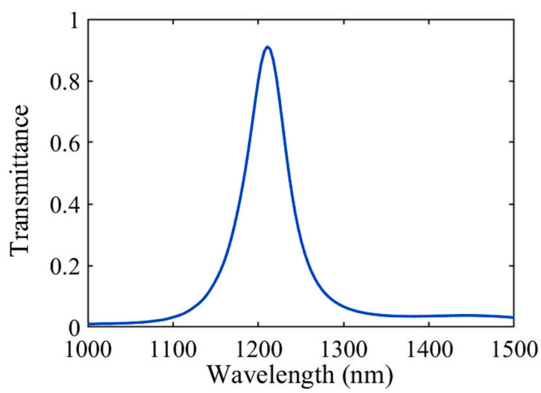

Fig. 3. Transmission spectrum of the proposed plasmonic band-pass filter. The device demonstrates a Gaussian-like resonance mode at the central wavelength of 1210 nm with a peak transmittance of 91%.

redshift of the resonance wavelength, which indicates a reduction in the energy required to excite surface plasmon polaritons (SPPs); however, this is accompanied by a degradation in the transmission coefficient. In Fig. 4(b), the 3D transmission curve is presented for variations in the width of the rectangular resonator (D) from 210 to 330 nm with a step size of 6 nm. It is evident that an increase in dimensions enhances the transmission coefficient and induces a blueshift in the transmission peaks, suggesting an increase in the energy required for SPP excitation. In Fig. 4(c), the 3D transmission curve is depicted for changes in the length of the rectangular resonator (L) from 440 to 560 nm with a step size of 6 nm. It is observed that increasing the dimensions leads to a shift in the resonance wavelength, while the transmission coefficient exhibits a non-monotonic behavior, initially increasing and subsequently decreasing.

It is essential to clarify that the spectral trends in Fig. 4 are governed by a combination of geometric and modal effects. While the radius R mainly scales the optical path length, leading to a consistent redshift, the rectangular dimensions D and L significantly alter the modal confinement and impedance matching of the SPP mode. The non-monotonic behavior observed for these parameters is a physical manifestation of the competition between resonant mode enhancement and the increased intrinsic propagation/scattering losses that occur as the resonator dimensions deviate from the optimal coupling condition.

Table 3 summarizes the parametric sensitivity analysis of the proposed resonator. To quantify the influence of geometric variations on the resonance condition, the sensitivity (S) is defined as $S = \Delta\lambda / \Delta param$. The results indicate that the resonator radius (R) is the most dominant factor affecting the resonance wavelength, exhibiting a high positive sensitivity of +2.22 nm/nm, which leads to a significant redshift. Conversely, the rectangular width (D) demonstrates a negative sensitivity of −0.69 nm/nm, inducing a blueshift due to the modulation of the effective refractive index and modal confinement. The resonator length (L) shows a moderate positive sensitivity of +0.30 nm/nm, contributing to a slight redshift. These quantitative findings confirm that the resonance wavelength can be precisely tuned by adjusting the geometric parameters, providing a clear roadmap for the design and optimization of the plasmonic filter and memory device.

The effect of the coupling gap between the input/output waveguides and the resonator is investigated in Fig. 5. The gap size is varied from 0 nm to 18 nm with a step size of 3 nm. It is observed that the transmission coefficient undergoes a progressive degradation as the gap dimension increases, indicating a strong dependence of the coupling efficiency on the spatial separation between the waveguide and the resonant cavity.

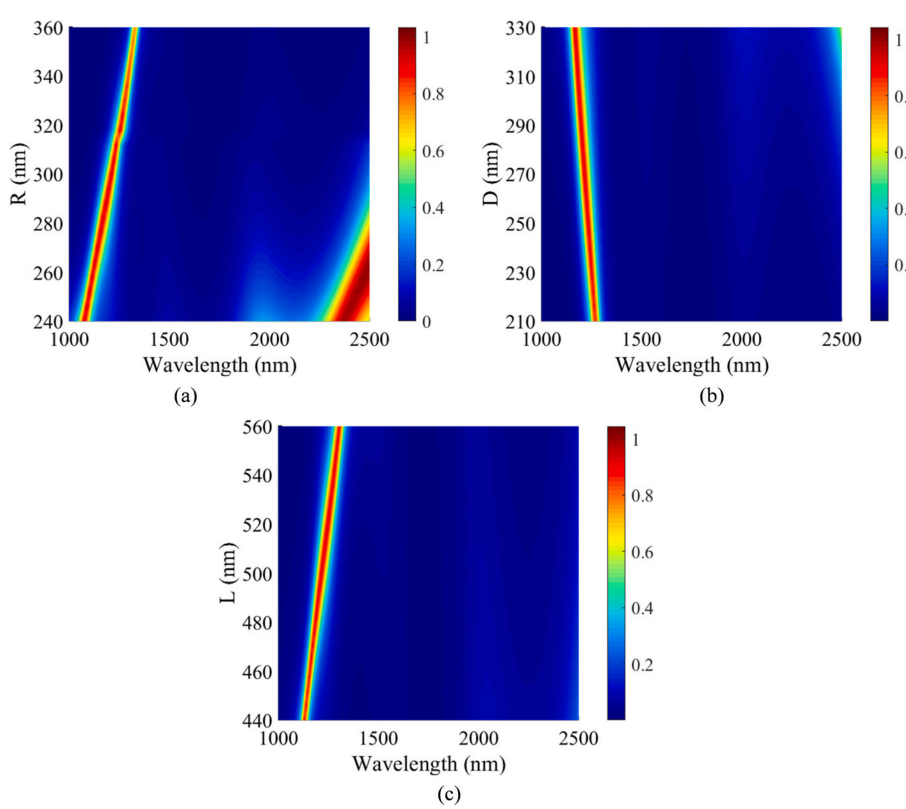

Fig. 4. Normalized transmission curves for dimensional variations of (a) R, (b) D, and (c) L.

Table 3
Parametric sensitivity analysis of the proposed dumbbell-shaped resonator. The sensitivity S is defined as Δλ / Δparam, where a positive value denotes a redshift and a negative value denotes a blueshift.

Parameter	Variation Range (nm)	Δλ (nm)	Sensitivity (nm/nm)	Trend
R	240–360	+267	+ 2.22	Red shift
D	210–330	−83	−0.69	Blue shift
L	440–560	+36	+0.3	Red shift

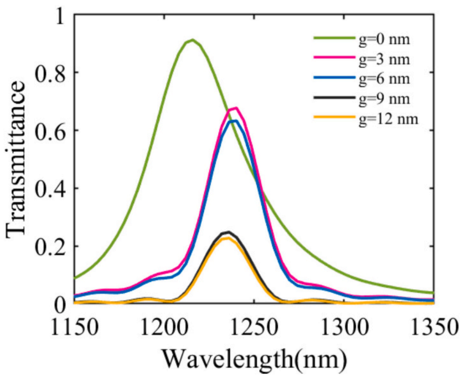

Fig. 5. Transmission variation curve as a function of the coupling gap (g).

The dependence of transmission on the coupling gap is governed by the evanescent coupling mechanism. As the waveguide and the resonator are brought into contact (g = 0 nm), the spatial overlap of their respective SPP modes is maximized, facilitating efficient energy transfer into the resonant cavity. As the gap increases, the evanescent field intensity at the resonator boundary decays exponentially, leading to a rapid decrease in the coupling efficiency. Additionally, the increased gap distance disrupts the phase matching and induces an impedance mismatch at the interface, which results in significant reflections and radiative losses. Thus, the observed transmission drop is a direct consequence of the diminished evanescent interaction and the degradation of the mode-coupling efficiency.

In plasmonic structures, evaluating the magnetic and electric fields at the resonance wavelength is essential. At this wavelength, the electric field of the surface plasmons at the silver-air interface is significantly enhanced, leading to the excitation of Surface Plasmon Polaritons (SPPs) (Taflove et al., 2005). Figs. 6(a) and 6(b) illustrate the magnetic field magnitude (|H|) and electric field magnitude (|E|) distributions at the resonance wavelength of 1210 nm, respectively.

The magnetic field profile of the filter structure in Fig. 6(a) demonstrates that the maximum energy is trapped within the central rectangular resonator, confirming energy storage, while energy conduction is facilitated through the semi-disk resonators. The electric field profile in Fig. 6(b) shows high-intensity field enhancement at the corners of the central rectangular resonator at the interface of the two materials. This enhancement, caused by the resonance of plasmon polaritons, indicates the potential suitability of this filter for sensing applications.

In this design, the refractive index of the surrounding dielectric (air) is varied from 1 to 1.05 in increments of 0.01. As shown in Fig. 7, a refractive index increase of 0.01 results in a resonance wavelength shift from 1210 nm to 1225 nm. This pronounced shift indicates the strong dependence of the spectral response on the effective refractive index of the plasmonic mode. Such behavior highlights the high tunability of the

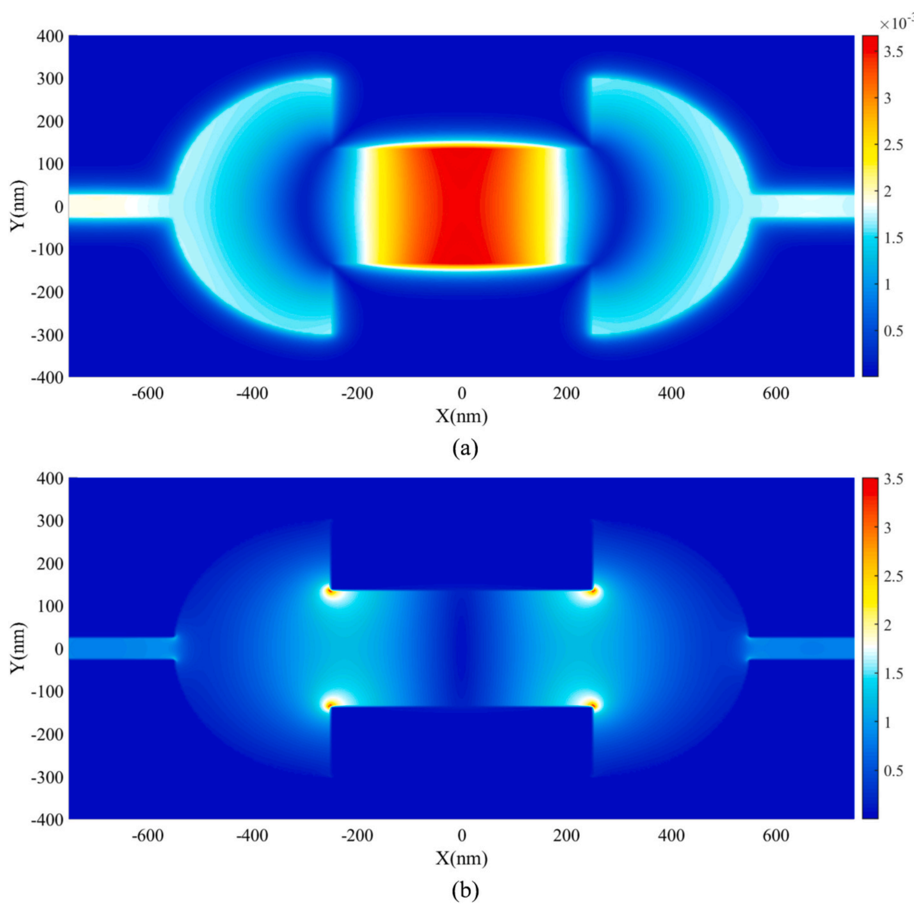

Fig. 6. Field distribution profiles: (a) Magnetic field magnitude (|H|), (b) Electric field magnitude (|E|).

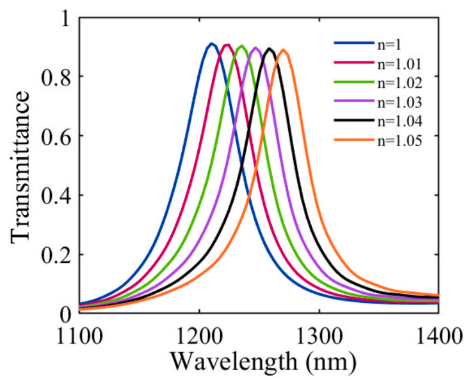

Fig. 7. Resonance wavelength shift induced by a 0.01 increment in refractive index.

proposed structure, enabling precise control and engineering of the resonance wavelength through the selection of dielectric materials with different refractive indices.

In plasmonic systems, several theoretical models are employed to describe the dielectric function of metals. In this study, the metal permittivity is described using the classical Drude model, which accounts for the free-electron response and provides an accurate approximation of the optical properties of metals in the considered wavelength range. To conduct a rigorous evaluation of the designed structure, the transmission curves obtained using the Drude theoretical model, the Johnson and Christy experimental model, and Palik data are compared in Fig. 8(a). The transmission curves derived from the Drude and Johnson/Christy models exhibit nearly perfect agreement at the resonance wavelength of 1210 nm with a transmittance of 91%, as shown in Fig. 8(b). In contrast, the transmission curve using Palik data shows a transmittance of 67% at a resonance wavelength of 1214 nm.

Thus far, the proposed filter structure, its operational mechanism, the optimization process of variable parameters, the effects of refractive index variations, and various metal dielectric models have been comprehensively analyzed.

Table 4 presents a comparative analysis of the proposed filter's critical performance metrics—including resonance wavelength (λ_0), peak transmission (T), FWHM, and the Quality factor (Q)—against previously reported plasmonic filters. To ensure physical consistency, the dielectric properties of silver were modeled using both the Drude and Johnson and Christy models; both approaches show excellent agreement at the resonance wavelength of 1210 nm, yielding an identical peak transmission of 91%. While minor variations in the FWHM are observed between these models, the proposed dumbbell-shaped structure consistently demonstrates a superior peak transmission and an enhanced Quality factor compared to existing literature. It should be noted that there exists a fundamental trade-off between transmission efficiency and the Quality factor in plasmonic resonators. Our design prioritizes high transmission to ensure optimal signal detection when integrated with phase-change materials for memory operations, where distinct discrimination between logic states '0' and '1' is required. These results confirm the structure's enhanced spectral selectivity and its potential for high-performance photonic applications.

Table 4 presents a comparative analysis of the proposed dumbbell-shaped filter against previously reported plasmonic resonators. It should be clarified that the filter presented here serves as the passive backbone for our proposed plasmonic memory architecture. In the design of such resonators, there is a fundamental trade-off between the transmission efficiency (T) and the Quality factor (Q). In this work, we deliberately prioritized high peak transmission (91%) over an ultra-high Q-factor. This design choice is critical for the intended integration of the GST phase-change material; since the active GST layer introduces significant optical losses during the phase-transition process, a high-transmission baseline is essential to compensate for these losses and maintain a clear signal-to-noise ratio for memory read-out operations.

4. Plasmonic memory

To achieve a non-volatile plasmonic memory, a phase-change material with dimensions L1 × D1 and a probe signal have been integrated into the plasmonic filter design. The optimized dimensions of the variable parameters for this memory are listed in Table 5. In this design, silver (Ag) is used as the metal, while air and GST phase-change material serve as the dielectrics. The Drude model is employed to characterize the metal's dielectric function, and the results are reported using the FDTD method. The schematic design of the non-volatile read-only plasmonic memory structure is shown in Fig. 9.

The operation of the memory structure is based on two independent optical signal pathways. The control signal, which comprises the set and reset pulses required for inducing phase transitions in the GST material, is applied to the structure from above the chip using a laser source, as depicted in the schematic of Fig. 9b. In contrast, the optical probe signal is guided through the input MIM waveguide to interrogate the memory state. The logic level ('0' or '1') is distinguished by detecting the transmission coefficient at the output MIM waveguide, where the contrast between the amorphous and crystalline phases provides the basis for signal read-out.

The programming of the memory structure is achieved through an external optical addressing approach, referred to as top-chip programming. As depicted in Fig. 9(b), SET and RESET pulses are applied as a top-illumination control signal, which induces the phase transition of the GST resonator via localized photothermal heating. This process is

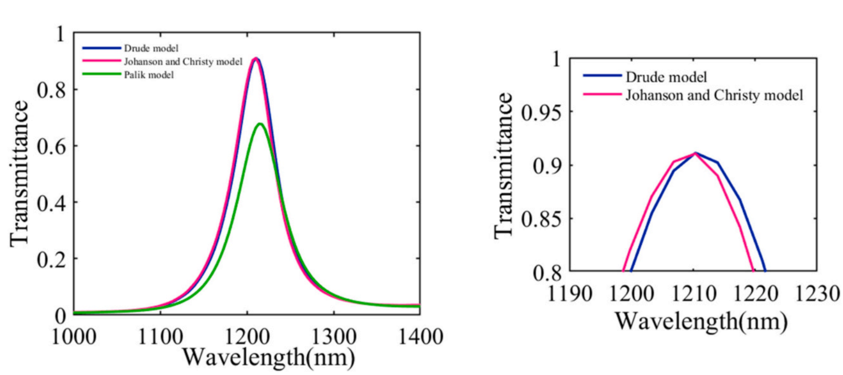

Fig. 8. (a) Comparison of the filter transmission curve using theoretical (Drude), experimental (Johnson-Christy), and Palik data; (b) Consistency between theoretical and experimental models.

Table 4
Comparison of the Proposed Filter Characteristics with Existing Literature.

Ref.	Year	Number of modes	Simulation model	λ_0 (nm)	Maximum Transmittance (%)	FWHM (nm)	Q-factor
(Hajshahvaladi et al., 2022)	2020	2	–	857, 541	85, 89.7	26.5, 82	20.4, 10.4
(Fonteyne et al., 2007)	2020	2	–	710, 1430	54, 51	–	–
(Heidari and Nozhat, 2022)	2022	2	Drude	1010, 1550	80, 70	28.6, –	35.27, –
(Shafagh et al., 2020)	2022	3	Johnson and Christy	700, 800, 860	74, 85, 86	–	14, 8, 8
(Hasan et al., 2020)	2023	2	–	1110, 1340	72, 77	–	–
(Zegaar et al., 2022)	2024	2	Johnson and Christy	1551, 761	22, 76	–	19.1
(Abd-Elsamee et al., n.d.)	2024	3	Coupled Mode Theory	61,580	–	8025	7.67
(Cui et al., 2023)	2024	1	Experimental	1430	79	–	–
(Yang et al., 2024)	2025	1	Drude	1148	89	114	10.3
Proposed Filter			Drude	1210	91	56	21.6
		1	Johnson and Christy	1210	91	57	21.2

Table 5
Dimensions of Variable Parameters for the Plasmonic Memory.

Parameter	R	L	D	g	L1	D1	d	W
Dimensions (nm)	300	500	270	0	500	190	40	50

spatially and functionally independent of the readout operation, which involves the propagation of a probe signal through the MIM waveguide. By decoupling the control and probe signals, the device enables efficient non-volatile logic state switching and robust high-contrast readout.

The programming of this memory is performed externally to the integrated circuit using a laser; specifically, a programming signal containing RESET and SET pulses is applied to the structure, performing the processes of writing logical states 0 and 1 into the memory, respectively.

The state stored in the memory is read by applying a low-power (low-amplitude) probe signal to the structure. This signal lacks the intensity to alter the refractive index or the state of the phase-change material and determines the stored state in the memory solely by comparing the transmission curves.

By applying the probe signal to the structure, the logic value written in the memory is read. Upon applying this signal, the transmission curves for both the amorphous and crystalline states of the GST material are illustrated in Fig. 10.

In the amorphous state, the transmission curve within the wavelength range of 1600–2200 nm exhibits a Gaussian-shaped transmission mode at the resonance wavelength of 1912 nm, featuring a transmittance of 95%. Conversely, in the crystalline state, the transmission curve is entirely zero. Thus, the memory read operation is performed within the structure. This non-volatile read-only memory is categorized as an active plasmonic device.

Consistent with the previous analysis, the 3D transmission spectra of the proposed GST-based rectangular resonator, in terms of the geometric variations of parameters D1 and L1, are illustrated in Fig. 5. Although these parameters are dependent on the global dimensions L and D, their individual optimization is crucial for achieving the desired memory performance.

Fig. 11(a) displays the 3D transmission curve as a function of the parameter D1. As D1 is increased from 160 nm to 220 nm with a step size

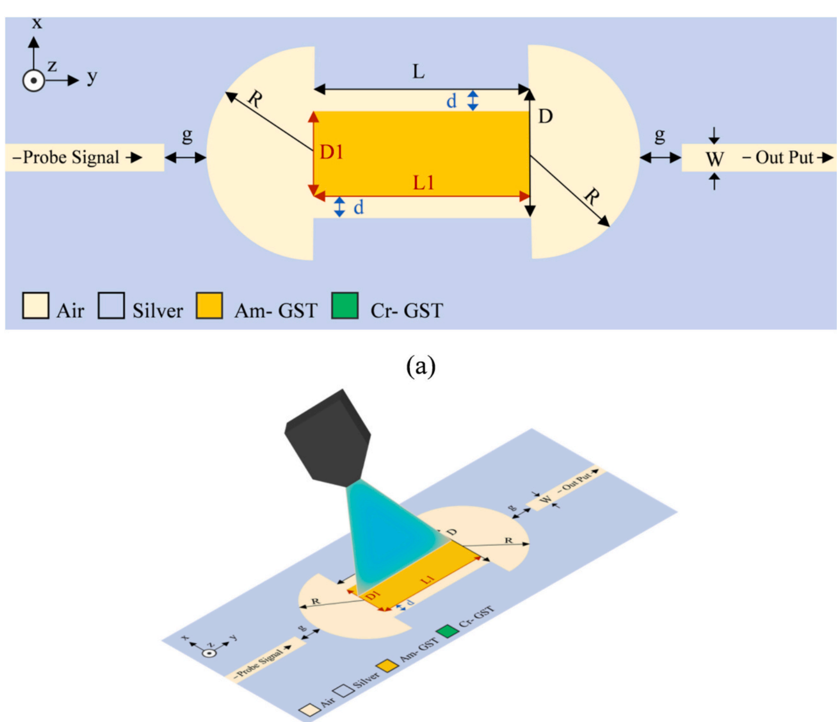

(a)

(b)

Fig. 9. (a) Schematic of the second read-only memory (ROM) structure design, (b) Memory programming based on phase-change GST material using laser excitation to induce reversible transitions between the amorphous and crystalline phases.

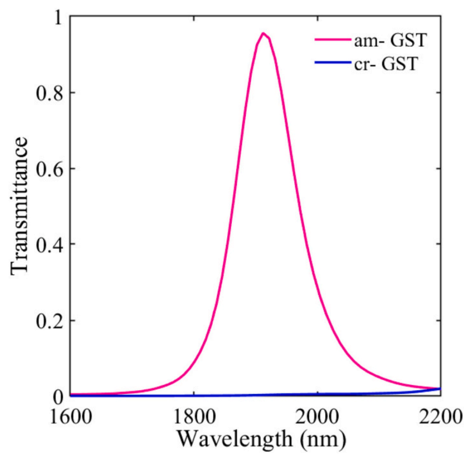

Fig. 10. Transmission curve of the memory structure upon application of the Probe signal.

of 3 nm, a clear redshift of the resonance wavelength is observed. Furthermore, the transmission coefficient exhibits a non-monotonic behavior, showing an initial enhancement up to 196 nm, followed by a subsequent decrease.

Similarly, the 3D transmission spectra of the proposed memory cell concerning the variation of parameter L1 is depicted in Fig. 11(b). In this case, L1 is varied from 470 nm to 530 nm with a step size of 6 nm. It is observed that increasing L1 leads to a simultaneous redshift of the resonance wavelength and an improvement in the transmission coefficient.

To evaluate the capability of the plasmonic memory in detecting states 0 and 1, and its ability to differentiate between them, it is essential to examine two factors: Contrast Ratio (CR) and Extinction Ratio (ER). These two factors can be calculated using eqs. (8) and (9), respectively.

$$\text{Contrast} = T_{am} - T_{cr} \tag{8}$$

$$\text{Extinction Ratio (dB)} = 10\log_{10}\frac{T_{am}}{T_{cr}} \tag{9}$$

$$\text{Storage Density}\left(\frac{\text{bits}}{\mu m^2}\right) = \frac{\text{Total Number of Bits}}{\text{Total Area } (\mu m^2)} \tag{10}$$

In Fig. 12(a), the contrast curve of the memory structure at the resonance wavelength of 1912 nm is illustrated, showing a 95% contrast between the amorphous and crystalline states. In Fig. 12(b), the extinction ratio curve at the resonance wavelength, which represents the memory structure's capability to differentiate between states 0 and 1, is measured at ER = 25 dB. This memory features Footprint = 0.095 μm^2 and 10.5 $\frac{bits}{\mu m^2}$ integration density, which has been calculated using Eq. (10). In the GST-based plasmonic memory, phase transition between amorphous and crystalline states is observed through the analysis of magnetic field distributions, while the energy transfer mechanism within the structure is visualized via electric field distributions (Taflove et al., 2005).

The proposed memory cell achieves an ultra-compact footprint of 0.095 μm^2, yielding a bit density of 10.5 bits/μm^2. This density is calculated based on the active GST-filled rectangular resonator area. A key design feature of our architecture is the use of air-filled regions for the surrounding plasmonic side resonators and MIM waveguides. These air-filled gaps not only provide a low-index background that facilitates superior field confinement within the GST layer but also minimize coupling losses and spatial crosstalk. Furthermore, the implementation of external top-chip optical programming eliminates the requirement for dense on-chip wiring, allowing for a scalable and dense memory array where photonic components are integrated within an air-gap topology to minimize the overall system footprint.

The magnetic field profile for reading logic state 1 is shown in Fig. 13 (a), where the application of the probe signal results in maximum resonance within the rectangular resonator containing the phase-change material. The electric field profile during the “read 1” operation is depicted in Fig. 13(b). The intense confinement of light in the resonators above and below the GST region demonstrates the structure's capability to transfer energy to the material and guide it toward the output waveguide.

The magnetic and electric field profiles for reading logic state 0 are shown in Figs. 14(a) and 14(b), respectively. It is demonstrated that upon applying the probe signal to the structure, the energy is absorbed due to the high losses of the GST material in its crystalline state, preventing transmission to the output waveguide.

To evaluate the propagation efficiency of the proposed memory cell at the resonance wavelength of 1912 nm, the insertion loss (IL) was calculated for both the amorphous (Logic ‘1’) and crystalline (Logic ‘0’) states using the relationship defined in Eq. (11).

$$\text{Insertion Loss (dB)} = -10\log_{10}T \tag{11}$$

As illustrated in Fig. 15, the device exhibits an IL of 0.19 dB for the amorphous state and 25.2 dB for the crystalline state. The remarkably low insertion loss in the amorphous state highlights the high propagation efficiency of the structure and its viability for large-scale, high-density photonic integration. Furthermore, this result demonstrates that the design effectively mitigates the impact of ohmic dissipation typically associated with metal-based plasmonic waveguides, confirming the robustness of the architecture for active signal processing.

The electromagnetic response of the proposed structure is governed by Maxwell's curl equations in the time domain (Wang et al., 2020):

$$\nabla \times E = -\mu\frac{\partial H}{\partial t} \tag{12}$$

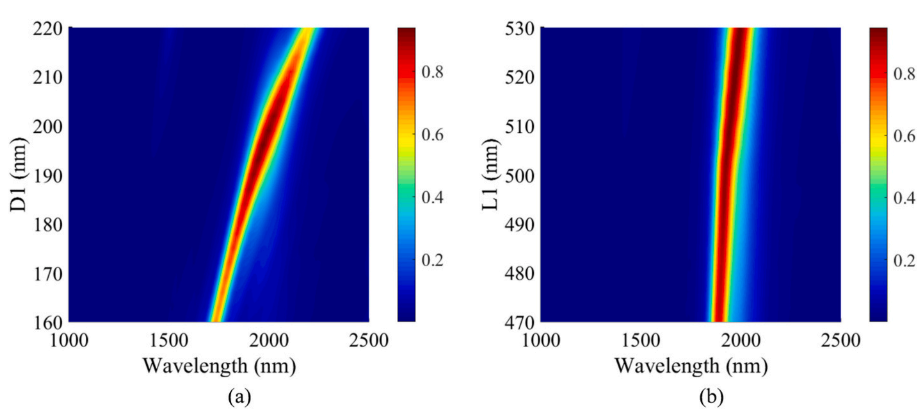

Fig. 11. Normalized transmission curves for dimensional variations of (a) D1, (b) L1.

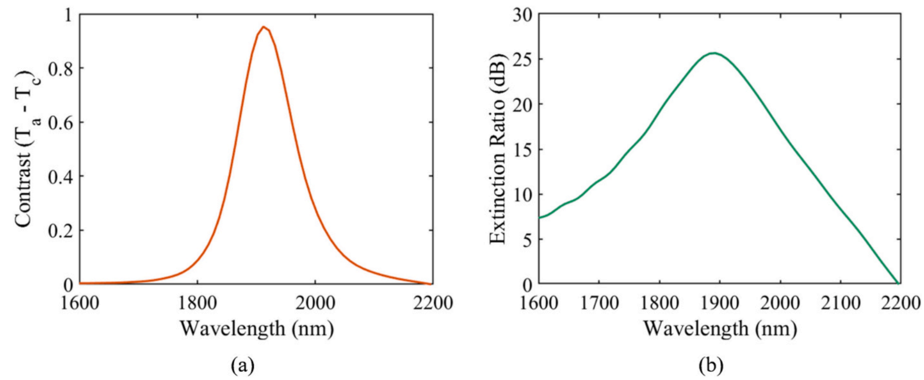

Fig. 12. Performance metric curves: (a) Optical Contrast, (b) Extinction Ratio (ER).

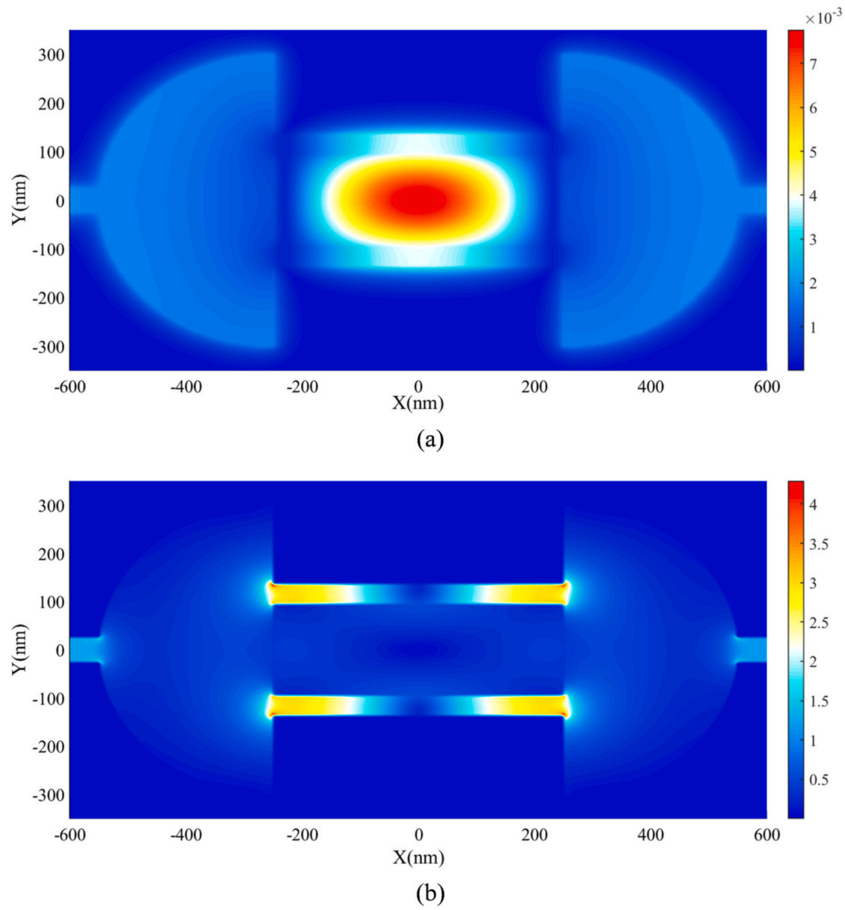

Fig. 13. Field distributions for logic states: (a) Magnetic field and (b) Electric field in "Read 1" state.

$$\nabla \times H = \varepsilon_0 \varepsilon_r \frac{\partial E}{\partial t} \tag{13}$$

where E and H are the electric and magnetic field vectors, μ_0 is the vacuum permeability, ε_0 is the vacuum permittivity, and ε_r represents the relative complex permittivity of the material. The volumetric power density Q generated by optical absorption within the GST cell is calculated as (Verma and Srivastava, 2024):

$$Q_{optical}(x, y, z) = \frac{1}{2}\omega\varepsilon_0 \mathrm{Im}(\varepsilon_r)|E|^2 \tag{14}$$

This optical power acts as a heat source in the Fourier heat conduction equation to determine the spatiotemporal temperature distribution T(t, r):

$$\rho C_p \frac{\partial T}{\partial t} = \nabla.((K\nabla T)) + Q_{optical} \tag{15}$$

where ρ, C_P, and K denote the density, specific heat capacity, and thermal conductivity of the GST, respectively (Korani et al., 2024). The crystalline volume fraction X ($0 \leq X \leq 1$) is then calculated using the Johnson-Mehl-Avrami-Kolmogorov (JMAK) kinetics:

$$X(t) = 1 - \exp(-[K_{JMAK}(T).t]^n) \tag{16}$$

with the crystallization rate constant k(T) defined by the Arrhenius activation relation:

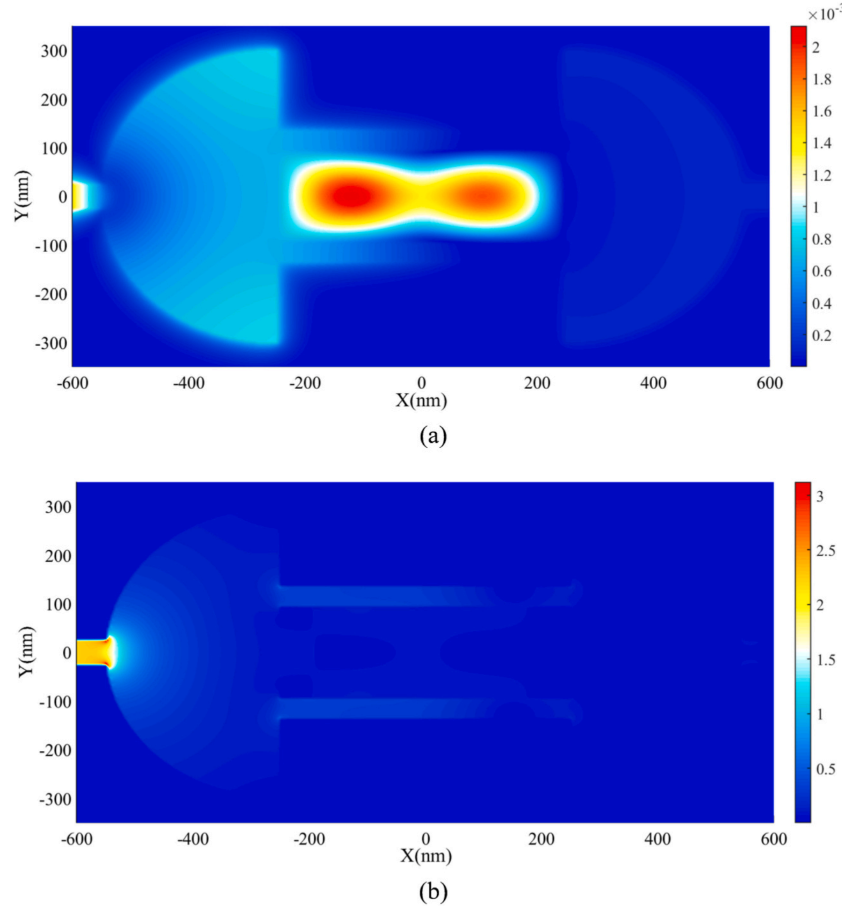

Fig. 14. Field distributions for logic states: (a) Magnetic field and (b) Electric field in "Read 0" state.

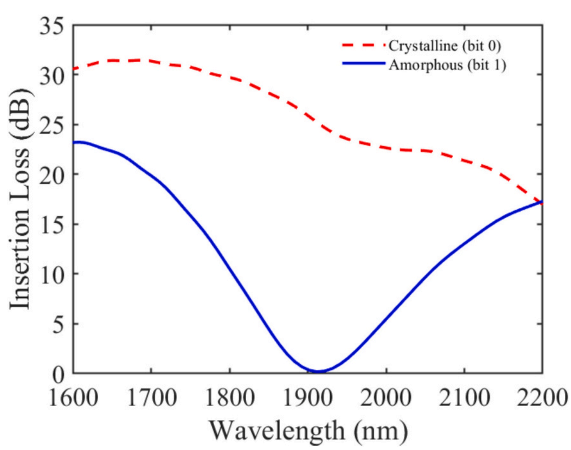

Fig. 15. Insertion loss (IL) spectrum in dB for the proposed structure during the amorphous and crystalline states of the GST medium at the 1912 nm resonance peak.

$$K_{JMAK}(T) = \nu \exp\left(-\frac{E_a}{k_B T}\right) \quad (17)$$

where n is the Avrami exponent, E_a is the activation energy, and ν is the pre-exponential factor (Kehtarmanesh et al., 2025). Finally, the dielectric function of the GST layer is updated using the Effective Medium Approximation (EMA) (Anopchenko et al., 2023; Stegmaier et al., 2016):

$$\widetilde{n}(x, y, z) = X.\widetilde{n_c} + (1 - X).\widetilde{n_a} \quad (18)$$

This multiphysics cycle, iterating between electromagnetic absorption, heat diffusion, and phase evolution, is integrated into our FDTD framework to ensure the physical consistency of the switching process.

Although the primary investigation of this device is focused on its photonic performance through FDTD simulations, the physical feasibility of the switching mechanism is rigorously justified by photothermal analysis. To provide a precise thermal justification of the structure, one can utilize the governing relations defined in this work. Specifically, the optical power density Q (Eq. 14) serves as the heat source term in the Fourier heat conduction equation (Eq. 15), incorporating the high thermal conductivity of the silver (Ag) layers and the surrounding dielectric environment. Furthermore, the phase transition kinetics, dictated by the Avrami equation (Eq. 16) and the Arrhenius activation relation (Eq. 17), determine the phase evolution (Eq. 18). These analytical relations confirm that the chosen SET/RESET pulse parameters—configured in alignment with reference (Zareizadeh and Nozhat, 2023)—are sufficient to induce a reversible phase transition while maintaining the structural integrity of the device.

While this study demonstrates the binary switching functionality of the proposed plasmonic memory, the device architecture is inherently compatible with multi-level weight modulation. The optical transmission is directly controlled by the complex refractive index of the GST layer; thus, the well-documented ability of GST to undergo fractional crystallization (Wuttig and Yamada, 2007; Rios et al., n.d.; Michel et al., 2014) enables intermediate phase states that correspond to analog synaptic weights. The physical feasibility of such transitions is rigorously supported by a photothermal framework where the optical power density $Q_{optical}$ (Eq. 14) serves as the heat source in the Fourier conduction equation (Eq. 15). Furthermore, the phase evolution kinetics, governed by the Avrami (Eq. 16) and Arrhenius (Eq. 17) relations, confirm that the SET/RESET pulse parameters are sufficient to induce precise phase changes. This analytical foundation ensures that our device serves as a robust platform for both binary logic and future analog neuromorphic applications.

5. Neuromorphic photonic performance and time-domain analysis

The neuromorphic functionality of the proposed plasmonic memory structure can be directly inferred from its phase-dependent optical response. The pronounced difference in optical transmission between the amorphous and crystalline states of GST enables controlled modulation of the output intensity, which can be mapped onto synaptic weights in neuromorphic systems. This behavior is further supported by the high optical contrast (95%) and extinction ratio (25 dB), ensuring clear discrimination between logic states. Specifically, the high-transmission state (amorphous phase) corresponds to a potentiated synaptic state, whereas the low-transmission state (crystalline phase) represents a depressed synaptic state. In addition, the transient responses observed in the time-domain analysis indicate the capability of gradual weight modulation rather than purely binary switching. This behavior, arising from the strong coupling between plasmonic resonance and phase-change dynamics, confirms that the proposed structure can function as an all-optical synaptic element for neuromorphic computing applications. Furthermore, the ultra-compact footprint (0.095 μm^2) enables high-density integration in photonic integrated circuits. The high storage density (10.5 bits/μm^2) further highlights the strong potential of the proposed architecture for on-chip neuromorphic and photonic information processing applications.

It should be noted that while this study demonstrates the binary switching functionality of the proposed plasmonic memory, the device structure is inherently compatible with multi-level weight modulation. The optical transmission of the proposed design is directly controlled by the phase state of the GST layer. Given the well-documented ability of GST to undergo fractional crystallization (Wuttig and Yamada, 2007; Rios et al., n.d.; Michel et al., 2014), intermediate phase states between the fully amorphous and fully crystalline levels can be achieved. These states are expected to provide continuous control over the optical transmission, thereby serving as a foundational platform for analog synaptic weight modulation in photonic neuromorphic networks. Exploring the specific kinetics of these intermediate states remains a significant direction for future research.

For the transient analysis, the excitation source is modeled as a time-normalized square pulse on a femtosecond scale. The pulse profile is defined by a null-power state for the initial 100 fs, a transition to unity magnitude spanning 100 fs to 800 fs, and a subsequent return to zero within the 800–1200 fs interval. By employing sharp rising and falling edges, this excitation scheme facilitates a precise assessment of the device's switching dynamics, including signal propagation delay, power attenuation, and overall temporal stability. The schematic of this excitation signal is shown in Fig. 16.

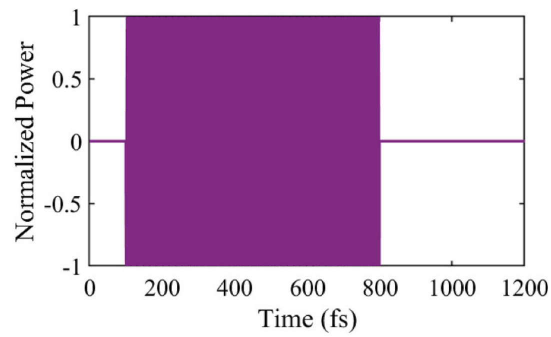

Fig. 16. Schematic of the excitation signal applied to the input waveguide for performing transient analysis in the dumbbell memory structure.

To quantify the propagation losses intrinsic to the input and output metal-insulator-metal (MIM) waveguides, a reference simulation was performed by launching the femtosecond excitation pulse into the waveguide channels in the absence of the GST-loaded dumbbell resonator. As depicted in Fig. 17(a), the output signal retrieved at the waveguide terminus exhibits a peak amplitude of 0.95, while the pulse profile remains nearly identical to the input excitation. This observation confirms that the utilized MIM waveguides provide low-loss signal propagation and preserve signal integrity without introducing substantial temporal distortion. Consequently, any deviations from the original temporal profile observed in the complete device architecture can be attributed solely to the light-matter interaction within the resonator and the phase-state of the GST layer.

When the GST material is switched to the amorphous state (logic state ‘1’), which exhibits a lower absorption coefficient compared to the crystalline phase, the output power—despite existing coupling losses—is depicted in Fig. 17(b). The output power exhibits an initial propagation delay (T_d) of 7 fs, followed by a gradual increase, reaching approximately 0.95 by 200 fs. This behavior is attributed to propagation delay, dispersion, and mode coupling effects, while the value below unity arises from initial coupling losses and modal mismatch. Within the 200–800 fs interval, a quasi-steady state is observed, indicating stable pulse propagation through the amorphous phase with limited losses.

Upon termination of the input pulse, the power gradually decays due to ohmic losses, reaching zero at approximately 1100 fs. Based on the quasi-steady state value of 0.95, the rise time (10% to 90% of steady-state) is calculated to be 82 fs, and the fall time (90% to 10%) is 84 fs.

Conversely, in the crystalline state (logic state ‘0’), induced by the SET control pulse, the increased refractive index and absorption coefficient of the GST layer significantly alter mode coupling and enhance propagation losses. The temporal response for this state is shown in Fig. 17(c). Beyond the initial 7 fs delay, an abrupt increase to 0.12 occurs at 107 fs, stemming from the transient excitation of parasitic modes and modal mismatch upon source activation. Within the 200–800 fs interval, the signal settles into a quasi-steady state of approximately 0.04, signifying an ‘OFF’ regime with limited leakage. A secondary power rise to ~0.08 is observed, likely resulting from internal reflections and back-propagating wave interference. Finally, the output power decays to zero by 1100 fs under the influence of higher ohmic losses. Based on the 0.04 steady-state value, the rise time and fall time are measured to be 2 fs and 48 fs, respectively.

It should be noted that the temporal responses presented here are independent of the material's phase-change kinetics. Instead, they reflect the electromagnetic impulse response of the plasmonic structure during the read-out operation, governed by the system's impulse response and the optical parameters associated with the pre-set phase of the GST material.

The temporal characteristics of the read operation are determined by the electromagnetic response of the plasmonic structure, as shown in Fig. 17. While our study focuses on the stationary optical states, the practical switching speed and endurance of the GST layer are supported by extensive experimental literature (Zhang et al., 2019), which reports endurance up to 10^6 cycles and switching frequencies between 1 and 10 MHz, confirming the suitability of this material for high-performance memory applications.

Table 6 presents a comparative performance analysis of the proposed dumbbell-shaped memory against various state-of-the-art optical architectures. This comparison encompasses both plasmonic and photonic crystal-based devices utilizing diverse modulation mechanisms, including GST and nonlinear Kerr-effect media.

Our proposed memory cell achieves superior performance at a resonance wavelength of 1912 nm. By systematically integrating spectral selectivity with phase-change functionality, the dumbbell-shaped configuration achieves a transmission contrast of 95% and an extinction ratio of 25 dB within an ultra-compact footprint of 0.095 μm^2.

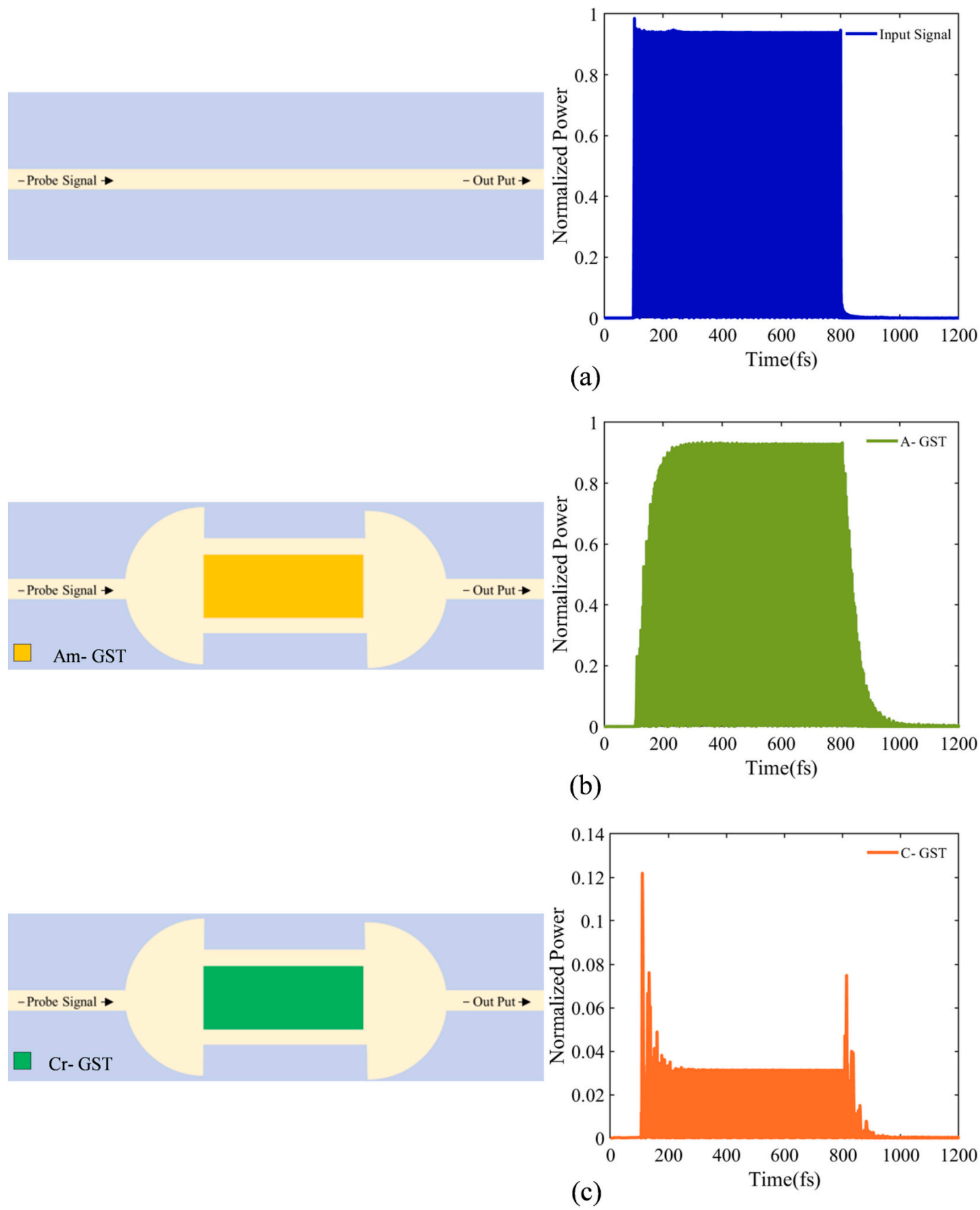

Fig. 17. Temporal response of the structure under excitation by a pulse with a square temporal profile mode: (a) plasmonic MIM waveguide in the reference state (without the memory structure) (b) read operation of logic state "1" (GST in the amorphous phase) (c) read operation of logic state "0" (GST in the crystalline phase).

Unlike conventional resonator geometries, this architecture facilitates highly localized field enhancement, effectively bridging plasmonic filtering and non-volatile memory functionalities to provide a robust advancement in high-density storage solutions. These metrics, derived from comprehensive FDTD simulations, intrinsically account for metallic dissipation, scattering, and mode-coupling effects within the MIM-GST configuration, demonstrating a clear performance advantage over existing plasmonic topologies.

6. Fabrication and structural integration

The proposed memory structure is engineered for compatibility with Back-End-of-Line (BEOL) Complementary Metal-Oxide-Semiconductor (CMOS) integration, utilizing standard nanofabrication protocols such as electron-beam evaporation, sputtering, electron-beam lithography (EBL), and reactive ion etching (RIE). The design employs an air-gap cavity configuration—a strategy widely adopted in integrated plasmonics to maximize light confinement—ensuring structural stability and dimensional accuracy consistent with established high-performance Metal-Insulator-Metal (MIM) resonators.

A critical design feature is the monolithic nature of the resonant cavity. In the optimized configuration, the coupling gap between the MIM waveguides and the resonator is fixed at 0 nm, allowing the entire resonant system to be patterned as a single continuous unit. This approach effectively bypasses the technical challenges associated with maintaining nanometer-scale alignment precision. The sensitivity analysis presented in Fig. 5, which examines gap variations from 0 nm to 18 nm, quantifies the impact of potential structural deviations—such as over-etching or lithographic inaccuracies—on the transmission coefficient. These results confirm that device performance is robust and

Table 6
Comparative analysis of key performance metrics for the proposed dumbbell-shaped plasmonic memory versus various plasmonic and photonic crystal-based memory architectures utilizing GST and nonlinear Kerr-effect materials.

Ref	Year	Material	Simulation	λ (nm)	Contrast (%)	ER (dB)	IL (dB)	Footprint (μm^2)	Density (bits/ μm^2)
(Du et al., 2022)	2020	Kerr	Plasmonic	708	64	10.06	1.48	0.83	1.2
(Skelton et al., 2012)	2020	Kerr	Plasmonic	755	62	15.05	1.93	0.23	4.3
(Youngblood et al., 2023)	2021	Kerr	Plasmonic	1485	49	12.38	2.83	0.31	3.2
(Khani et al., 2020a)	2022	GST	Plasmonic	1550	15.8	–	1.3	0.0045	222.2
(Khani et al., 2020b)	2025	GST	Plasmonic	1598	67	–	–	0.031	32.2
(Karimi et al., 2021)	2025	GST	Plasmonic	1178	74	–	–	0.14	7.1
(Sun et al., n.d.)	2025	GST	Plasmonic	1550	47	4.1	4.1	–	–
(Sharifipour et al., 2025a)	2025	Kerr	Plasmonic	830	68.6	–	–	1.2	0.83
(Sharifipour et al., 2025b)	2025	Kerr	Photonic Crystal	1550	66.6	–	–	30	0.03
(Anusha et al., 2026)	2026	GST	Photonic Crystal	1550	80	0.28	49	14.8	0.06
(Jafari and Danaie, 2025a)	2026	GST	Plasmonic	1776	84	43.66	Read: amorphous:7.86 crystalline:27.86	0.09	11.11
[86]	2026	GST	Plasmonic	1814	87	44.04	1-bit: Read: amorphous:0.60 crystalline:45.60	0.219	4.5
Proposed Memory		GST	Plasmonic	1912	95	25	Read: amorphous:0.19 crystalline:25.2	0.095	10.5

reaches its peak at the zero-gap configuration, validating the architecture for monolithic fabrication without the need for sub-10 nm alignment.

To ensure long-term environmental stability and prevent the oxidation of silver elements, the device can be encapsulated with ultra-thin dielectric passivation layers, such as Silicon Dioxide (SiO_2) or Aluminum Oxide (Al_2O_3), which provide protection without compromising plasmonic confinement. Furthermore, the design flexibility allows for the adoption of other CMOS-compatible materials by re-optimizing geometric parameters to maintain peak performance for switching operations (Jafari and Danaie, 2025a).

Finally, thermal management is intrinsically addressed by the device architecture. The high thermal conductivity of the silver substrate serves as an efficient passive heat sink for the active Germanium-Antimony-Tellurium (GST) layer. Coupled with the nanosecond-scale duration of the control pulses—which restricts the energy deposited into the deep-subwavelength volume of the GST resonator—this rapid heat dissipation prevents thermal crosstalk and ensures the structural reliability required for repeatable, high-fidelity switching between logic states '0' and '1'.

7. Conclusion

In this paper, we have reported the design and analysis of a single-mode plasmonic bandpass filter and a non-volatile plasmonic memory cell based on phase-change material (PCM). Through rigorous numerical evaluation, we demonstrated that the proposed structures achieve superior performance metrics—including high transmission contrast, a robust extinction ratio, and an ultra-compact footprint—that compare favorably with existing plasmonic topologies. While this study primarily validates the binary operational stability of the proposed memory cell, the device architecture provides a robust foundational platform for neuromorphic applications. The optical transmittance of the resonator, which is fundamentally governed by the complex refractive index of the GST layer, is intrinsically sensitive to the material's phase state. By leveraging the well-documented capability of PCM-based devices to undergo fractional crystallization, this architecture holds the potential to support multi-level transmission states. Such analog tunability is a prerequisite for implementing synaptic weight modulation. Consequently, the proposed device serves as a scalable building block for all-optical neuromorphic synapses, where the optical transmittance functions as a variable synaptic weight. This framework offers a clear path toward reproducing advanced learning dynamics, such as Spike-Timing-Dependent Plasticity (STDP), by employing tailored pulse-programming sequences to modulate the device's transmission levels in future neuromorphic circuits.

CRediT authorship contribution statement

Melina Kehtarmanesh: Writing – original draft, Software, Investigation, Data curation. **Parviz Keshavarzi:** Validation, Supervision, Project administration. **Mohammad Danaie:** Writing – review & editing, Validation, Supervision, Project administration, Conceptualization.

Ethical approval statement

The authors confirm that the submitted paper has not been submitted to any other journal and that this version is original and has not been published elsewhere. Additionally, all listed authors affirm the integrity of the study, data, information, and analyses, ensuring that no manipulations have been made. Furthermore, we confirm that no other individuals meet the authorship criteria for this paper beyond those listed as authors.

Funding

The authors declare that no funds, grants, or financial support were received for the preparation of this manuscript.

Declaration of competing interest

The authors declare that they have no known competing financial interests or personal relationships that could have appeared to influence the work reported in this paper.

Data availability

Data will be made available on request.

References

Abd-Elsamee S, Areed NF, El-Mikati HA, Obayya SS. Tunable multi-channels bandpass InGaAsP plasmonic filter using coupled arrow shape cavities. InPhotonics 2022 Oct 2 (Vol. 9, No. 10, p. 720). MDPI.

Ahmadivand, A., Gerislioglu, B., Sinha, R., Karabiyik, M., Pala, N., 2017. Optical switching using transition from dipolar to charge transfer plasmon modes in Ge2Sb2Te5 bridged metallodielectric dimers. Scientific reports. 7 (1), 42807.

Anopchenko, A., Gurung, S., Bej, S., Lee, H.W., 2023. Field enhancement of epsilon-near-zero modes in realistic ultrathin absorbing films. Nanophotonics 12 (14), 2913–2920.
Anusha, P., Srihari, K., Karthik, S., 2026. Reconfigurable plasmonic waveguides based on phase-change materials for on-chip optical switching. Plasmonics 21 (1), 1415–1424.
Bhatt, N., Parveen, S., Whab, A., munga P., 2024. Reduction of write current with improved thermal stability in GeSe2 doped Sb2Te3 films for phase change memory applications. Journal of Physics D: Applied Physics. 57 (36), 365306.
Blakemore, J.S., 1985. Solid state physics. Cambridge university press.
Butt, M.A., 2025. Plasmonic sensor system embedded with orthogonal mode couplers for simultaneous monitoring of temperature and refractive index. Plasmonics 20 (1), 459–469.
Chen, B., Ten Brink, G.H., Palasantzas, G., Kooi, B.J., 2017. Crystallization kinetics of GeSbTe phase-change nanoparticles resolved by ultrafast calorimetry. The Journal of Physical Chemistry C. 121 (15), 8569–8578.
Cui, Y., Jing, J., Dong, C., Qi, M., Gao, H., 2021. The influence of SOA on working memory guidance of attention. Journal of Cognitive Psychology. 33 (8), 853–860.
Cui, P., Huo, Y., Zhang, Z., Wang, Y., Song, M., Zhao, C., Liu, T., Liao, Z., 2023. Band-stop filter and narrow band-pass filter based on metal-insulator-metal waveguide. Micro and Nanostructures. 1 (175), 207503.
Dolatabady, A., Granpayeh, N., 2015. L-shaped filter, mode separator and power divider based on plasmonic waveguides with nanocavity resonators. IET Optoelectronics. 9 (6), 289–293.
Du, J., Zhou, J., Zhang, L., Yang, N., Ding, X., Zhang, J., 2022. Investigation of the crystallization characteristics of intermediate states in Ge2Sb2Te5 thin films induced by nanosecond multi-pulsed laser irradiation. Nanomaterials 12 (3), 536.
Ehrmann, A., Blachowicz, T., Ehrmann, G., Grethe, T., 2022. Recent developments in phase-change memory. Applied Research. 1 (4), e202200024.
Fonteyne, R., Buglioni, G., Leonori, I., O'Neill, F.G., 2007. Review of mesh measurement methodologies. Fisheries Research. 85 (3), 279–284.
Galoppo, M., Gaur, R., Harvey-Hawes, C., 2025. Kerr-Newman memory effect. Physical Review D. 111 (6), 064041.
Gemo, E., Carrillo, S.G., De Galarreta, C.R., Baldycheva, A., Hayat, H., Youngblood, N., Bhaskaran, H., Pernice, W.H., Wright, C.D., 2019. Plasmonically-enhanced all-optical integrated phase-change memory. Optics express. 27 (17), 24724–24737.
Gupta, R., Dwivedi, R.P., Sbeah, Z.A., Sorathiya, V., Alwabli, A., Alghamdi, A., Faragallah, O.S., 2025. GST and MXene-based highly sensitive refractive index sensor with gold gratings resonator operating for infrared region. Plasmonics 20 (6), 3067–3083.
Haddad, E., Kruzelecky, R.V., Murzionak, P., Jamroz, W., Tagziria, K., Chaker, M., Ledrogoff, B., 2022. Review of the VO2 smart material applications with emphasis on its use for spacecraft thermal control. Frontiers in Materials. 15 (9), 1013848.
Haffner, C., Heni, W., Fedoryshyn, Y., Niegemann, J., Melikyan, A., Elder, D.L., Baeuerle, B., Salamin, Y., Josten, A., Koch, U., Hoessbacher, C., 2015. All-plasmonic Mach–Zehnder modulator enabling optical high-speed communication at the microscale. Nature Photonics. 9 (8), 525–528.
Hajshahvaladi, L., Kaatuzian, H., Danaie, M., 2022. A high-sensitivity refractive index biosensor based on Si nanorings coupled to plasmonic nanohole arrays for glucose detection in water solution. Optics Communications. 1 (502), 127421.
Hao, Q., Cai, M., Dai, H., Xing, Y., Chen, H., Zhang, A., Li, L., Chenwen, Z., Wang, X., Han, J.B., 2024. All-in-One Magneto-optical Memory Arrays Based on a Two-Dimensional Ferromagnetic Materials. ACS Applied Materials & Interfaces. 16 (45), 62429–62435.
Haokang Z, Yichi P, Lingjie L, Wei L, Chong S, Dekun Y. Design of LSPR optical memory based on angle-resolved scattering measurement. In 2025 26th International Conference on Electronic Packaging Technology (ICEPT) 2025 (pp. 1-5). IEEE.
Hasan, M., Mayoa, F., Hossain, M.S., Ahmed, R., Hossain, M., Ali, K., Islam, S., 2020. Plasmonic corrugated waveguide coupled to a rectangular nano-resonator as an optical filter. OSA Continuum. 3 (12), 3314–3323.
He, Y., Farmakidis, N., Aggarwal, S., Dong, B., Lee, J.S., Wang, M., Zhang, Y., Parmigiani, F., Bhaskaran, H., 2024. Energy-efficient integrated electro-optic memristors. Nano Letters. 24 (51), 16325–16332.
Heidari S, Nozhat N. Plasmonic wideband GST-based switch in the near-infrared region. IET Optoelectronics. 2022;16(5):201-6.
Jafari, D., Danaie, M., 2025a. All-optical memory based on surface plasmons and kerr-type nonlinear cavity. Results in Physics. 1 (74), 108301.
Jafari, D., Danaie, M., 2025b. Ultra-fast all-optical memory based on hexagonal photonic crystal lattice on a GaAs substrate. e-Prime-Advances in Electrical Engineering. Electronics and Energy. 1 (12), 101034.
Jiang, W., Cheng, F., Xu, J., Wan, H., 2018. Compact and low-crosstalk mode (de) multiplexer using a triple plasmonic-dielectric waveguide-based directional coupler. Journal of the Optical Society of America B. 35 (10), 2532–2540.
Johnson, P.B., Christy, R.W., 1972. Optical constants of the noble metals. Physical review B. 6 (12), 4370.
Kang, Q., Li, D., Guo, K., Gao, J., Guo, Z., 2021. Tunable thermal camouflage based on GST plasmonic metamaterial. Nanomaterials 11 (2), 260.
Karimi, Y., Kaatuzian, H., Tooghi, A., Danaie, M., 2021. All-optical plasmonic switches based on Fano resonance in an X-shaped resonator coupled to parallel stubs for telecommunication applications. Optik 243, 167424.
Kehtarmanesh, M., Orouji, A.A., Keshavarzi, P., Danaie, M., 2025. Design of a single-mode plasmonic bandpass filter utilizing disk and elliptic resonators in a floral configuration. Physica Scripta. 100 (5), 055539.
Khani, S., Danaie, M., Rezaei, P., 2020a. All-optical plasmonic switches based on asymmetric directional couplers incorporating Bragg gratings. Plasmonics 15 (3), 869–879.
Khani, S., Danaie, M., Rezaei, P., 2020b. Compact and low-power all-optical surface plasmon switches with isolated pump and data waveguides and a rectangular cavity containing nano-silver strips. Superlattices and Microstructures. 1 (141), 106481.
Korani, N., Abbasi, A., Danaie, M., 2024. Band-pass and band-stop plasmonic filters based on Wilkinson power divider structure. Plasmonics 19 (2), 733–742.
Maier, S.A., 2007 May 16. Plasmonics: fundamentals and applications. Springer, New York.
Mcoyi, M.P., Mpofu, K.T., Sekhwama, M., Mthunzi-Kufa, P., 2025. Developments in localized surface plasmon resonance. Plasmonics 20 (7), 5481–5520.
Michel, A.K., Zalden, P., Chigrin, D.N., Wuttig, M., Lindenberg, A.M., Taubner, T., 2014. Reversible optical switching of infrared antenna resonances with ultrathin phase-change layers using femtosecond laser pulses. Acs Photonics. 1 (9), 833–839.
Moon, B.J., Song, Y.S., Son, D., Yang, H.Y., Bae, S., Lee, S.K., Lee, S.H., Kim, T.W., 2023. Implementation of Photosynaptic and Electrical Memory Functions in Organic Nano-Floating-Gate Transistors via a Perovskite-Nanocrystal-Based Nanocomposite Tunneling Layer. Small Science. 3 (9), 2300068.
Nikitin, A.A., Ryabcev, I.A., Nikitin, A.A., Kondrashov, A.V., Semenov, A.A., Konkin, D. A., Kokolov, A.A., Sheyerman, F.I., Babak, L.I., Ustinov, A.B., 2022. Optical bistable SOI micro-ring resonators for memory applications. Optics Communications. 15 (511), 127929.
Nohoji, A.H., Keshavarzi, P., Danaie, M., 2025a. Silicon-based all-optical photonic crystal neuromorphic synapses using Ge2Sb2Te5. Optics Continuum. 4 (8), 1591–1609.
Nohoji, A.H., Keshavarzi, P., Danaie, M., 2025b. Low-power all-optical photonic crystal synapse using Ge2Sb2Te5 phase-change material. Results in Optics. 25, 100901.
Nohoji, A.H., Keshavarzi, P., Danaie, M., 2026. All-Optical photonic crystal neuromorphic synapses using phase change material. Analog Integrated Circuits and Signal Processing. 126 (1), 13.
Oshita, M., Saito, S., Kan, T., 2023. Electromechanically reconfigurable plasmonic photodetector with a distinct shift in resonant wavelength. Microsystems & Nanoengineering. 9 (1), 26.
Palik, E.D., 1998. Handbook of optical constants of solids. Academic press.
Pan, Y., Chen, F., Li, Y., Yang, W., Sun, L., Yi, Z., 2024. A carbon nanotube metamaterial sensor showing slow light properties based on double plasmon-induced transparency. Physical Chemistry Chemical Physics. 26 (22), 16096–16106.
Park C, Sik Kang H. PCS Direct Communication for Low-Latency Optical Memory Interconnection. InSolar, Lighting and Thermal Photonics 2025 Jul 13 (pp. JTu3A-10). Optica Publishing Group.
Pomianowski, M., Heiselberg, P., Zhang, Y., 2013. Review of thermal energy storage technologies based on PCM application in buildings. Energy and Buildings. 1 (67), 56–69.
Prajapati, D.G., Kandasubramanian, B., 2020. A review on polymeric-based phase change material for thermo-regulating fabric application. Polymer Reviews. 60 (3), 389–419.
Pugachov, Y., Gulitski, M., Malka, D., 2024. Design of all-optical d flip flop memory unit based on photonic crystal. Nanomaterials 14 (16), 1321.
Qu Y, Li Q, Du K, Cai L, Lu J, Qiu M. Dynamic thermal emission control based on ultrathin plasmonic metamaterials including phase-changing material GST. Laser & Photonics Reviews. 2017;11(5):1700091.
Rahad, R., Ali, A., Pias, M.K., Farabi, M., Islam, M.A., Fahim, A.A., 2024. Plasmonic metal-insulator-metal (MIM) refractive index sensor for glucose level monitoring. Plasmonics 19 (5), 2605–2614.
Redaelli, A., Petroni, E., Annunziata, R., 2022. Material and process engineering challenges in Ge-rich GST for embedded PCM. Materials Science in Semiconductor Processing. 137, 106184.
Rios, C., Hosseini, P., Wright, C.D., Bhaskaran, H., Pernice, W.H., 2014. On-chip photonic memory elements employing phase-change materials.
Ruhul Fatin, M.A., Gostimirovic, D., Ye, W.N., 2024. Reconfigurable optical logic in silicon platform. Scientific Reports. 14 (1), 5950.
Shafagh, S.G., Kaatuzian, H., Danaie, M., 2020. Analysis, design and simulation of MIM plasmonic filters with different geometries for technical parameters improvement. Communications in Theoretical Physics. 72 (8), 085502.
Sharifipour, O., Keshavarzi, P., Danaie, M., 2025a. An ultra-compact low-power all-optical GST-based plasmonic switch for non-volatile neuromorphic synapses based on triangular cavity. Physica Scripta. 100 (8), 085563.
Sharifipour, O., Keshavarzi, P., Danaie, M., 2025b. All-optical plasmonic synapse based on phase change material suitable for neuromorphic circuits. Optical and Quantum Electronics. 57 (6), 356.
Shen X, Chen Y, Wang G, Lv Y. Phase-change memory and optical data storage. In Springer Handbook of Glass 2019 (pp. 1495-1520). Cham: Springer International Publishing.
Skelton, J.M., Loke, D., Lee, T.H., Elliott, S.R., 2012. Understanding the multistate SET process in Ge-Sb-Te-based phase-change memory. Journal of Applied Physics. 112 (6).
Song J, Pady J, Bente I, Pernice WH, Bhaskaran H, Wright CD. Plasmonically-enhanced phase-change integrated photonic memory device. InThe European Conference on Lasers and Electro-Optics 2025 Jun 23 (p. jsi_p_17). Optica Publishing Group.
Sreekanth, K.V., Medwal, R., Das, C.M., Gupta, M., Mishra, M., Yong, K.T., Rawat, R.S., Singh, R., 2021. Electrically tunable all-PCM visible plasmonics. Nano Letters 21 (9), 4044–4050.
Stegmaier, M., Rıos, C., Bhaskaran, H., Pernice, W.H., 2016. Thermo-optical effect in phase-change nanophotonics. Acs Photonics. 3 (5), 828–835.
Sun W, Lan D, Zhong Y, Qu X, Cheng Y. Lasp-2: Rethinking sequence parallelism for linear attention and its hybrid. arXiv preprint arXiv:2502.07563. 2025.
Sun W, Lu Y, Miao L, Zhang Y. All-optical phase-change memory with improved performance by plasmonic effect. InPhotonics 2022 Feb 25 (Vol. 9, No. 3, p. 132). MDPI.

Taflove, A., Hagness, S.C., Piket-May, M., 2005. Computational electromagnetics: the finite-difference time-domain method. The Electrical Engineering Handbook. 3 (629–670), 15.
Verma, S.K., Srivastava, S.K., 2024. Experimental demonstration of a Fano resonant hybrid plasmonic metasurface absorber for the O and E bands of the optical communication window. Journal of the Optical Society of America B. 41 (2), 356–363.
Wang, G., Nie, Q., Shen, X., Wang, R.P., Wu, L., Fu, J., Xu, T., Dai, S., 2012. Phase change behaviors of Zn-doped Ge2Sb2Te5 films. Applied Physics Letters. 101 (5).
Wang, N., Zhang, H., Zhou, L., Lu, L., Chen, J., Rahman, B.M., 2019. Design of ultra-compact optical memristive switches with GST as the active material. Micromachines 10 (7), 453.
Wang, G., Shi, H., Lotnyk, A., Shi, D., Wang, R., 2020. Conversion of p–n conduction type by spinodal decomposition in Zn-Sb-Bi phase-change alloys. NPG asia Materials. 12 (1), 17.
Wang, Q., Luo, R., Wang, Y., Fang, W., Jiang, L., Liu, Y., Wang, R., Dai, L., Zhao, J., Bi, J., Liu, Z., 2023. Set/Reset bilaterally controllable resistance switching Ga-doped Ge2Sb2Te5 long-term electronic synapses for neuromorphic computing. Advanced Functional Materials. 33 (19), 2213296.
Wang, Y., Chen, L., Wu, B., Wang, J., Fu, T., Xie, X., Xu, Y., Zhang, B., Li, J., Fan, L., Yang, X., 2026. Dual-mode optoelectronic neuromorphic memory for complex edge detection and recognition. Advanced Functional Materials. 36 (7), e14949.
West, P.R., Ishii, S., Naik, G.V., Emani, N.K., Shalaev, V.M., Boltasseva, A., 2010. Searching for better plasmonic materials. Laser & photonics reviews. 4 (6), 795–808.
Wuttig, M., Yamada, N., 2007. Phase-change materials for rewriteable data storage. Nature materials. 6 (11), 824–832.
Yang, X., Xu, H., Xu, H., Li, M., Yu, H., Cheng, Y., Chen, Z., 2024. Terahertz refractive index sensor based on dual plasmon-induced transparency in a graphene metasurface. Physica Scripta. 99 (5), 055518.
Yao, Y., Sang, D., Zou, L., Wang, Q., Liu, C., 2021. A review on the properties and applications of WO3 nanostructure-based optical and electronic devices. Nanomaterials 11 (8), 2136.
Youngblood, N., Rios Ocampo, C.A., Pernice, W.H., Bhaskaran, H., 2023. Integrated optical memristors. Nature Photonics. 17 (7), 561–572.
Zareizadeh, A., Nozhat, N., 2023. GST plasmonic gap structure investigation as a switch and sensor. Applied Optics. 62 (23), 6156–6162.
Zayets V, Serdeha I, Grygoruk V. Challenges of design and fabrication technology of plasmonic components for Photonic Integrated Circuits. InIntegrated Optics: Devices, Materials, and Technologies XXVI 2022 Mar 5 (Vol. 12004, pp. 163-171). SPIE.
Zegaar, I., Hocini, A., Harhouz, A., Khedrouche, D., Salah, H.B., 2022. Design of a double-mode plasmonic wavelength filter using a defective circular nano-disk resonator coupled to two MIM waveguides. Prog. Electromagn. Res. Lett. 1 (104), 67–75.
Zhang, J., Zhang, L., Xu, W., 2012. Surface plasmon polaritons: physics and applications. Journal of Physics D: Applied Physics. 45 (11), 113001.
Zhang, M., Pu, M., Zhang, F., Guo, Y., He, Q., Ma, X., Huang, Y., Li, X., Yu, H., Luo, X., 2018. Plasmonic metasurfaces for switchable photonic spin–orbit interactions based on phase change materials. Advanced Science. 5 (10), 1800835.
Zhang, H., Zhou, L., Lu, L., Xu, J., Wang, N., Hu, H., Rahman, B.A., Zhou, Z., Chen, J., 2019. Miniature multilevel optical memristive switch using phase change material. Acs Photonics. 6 (9), 2205–2212.